Environmental Pollution and Management 3 (2026) 202–213

Contents lists available at ScienceDirect

Environmental Pollution and Management

journal homepage: www.keaipublishing.com/en/journals/epm

Engineered Fe_3O_4/MgO/activated carbon nanocomposites as bifunctional materials for environmental remediation

Muhammad Zainullah[a], Mina Devika Setiana[a], Febriana Rahmawati[a], Alfi Qoidatul Rokhimah[a], Aura Gitta Zhafirah[a], Nurul Hidayat[a], Tahta Amrillah[b], Yap Wing Fen[c], Ahmad Taufiq[a,*]

[a] Department of Physics, Faculty of Mathematics and Natural Sciences, Universitas Negeri Malang, Malang 65145, Indonesia
[b] Department of Nanotechnology Engineering, Faculty of Advanced Technology and Multidiscipline, Universitas Airlangga, Surabaya 60115, Indonesia
[c] Department of Physics, Faculty of Sciences, Universiti Putra Malaysia, Selangor 43400, Malaysia

ARTICLE INFO

Keywords:
Fe_3O_4/MgO/AC (FOMAC)
Nanocomposites
Antibacterial agent
Adsorption efficiency
Environmental remediation

ABSTRACT

In recent years, increased industrial activity, without adequate wastewater management, has significantly contributed to rising levels of bacterial and heavy metal contamination in environments. Therefore, effective solutions for environmental remediation are required, particularly using economical, effective, efficient, and environmentally friendly. To address this issue, this research developed magnetite/magnesium oxide/activated carbon (Fe_3O_4/MgO/AC, FOMAC) nanocomposites that integrate dual functionalities within a single system, offering a more efficient and practical alternative compared to conventional materials. Interestingly, the Fe_3O_4 and AC nanoparticles were derived from natural materials, iron sand and coconut shells, which are environmentally friendly materials that contribute to reducing toxic reagents, decreasing environmental footprints, and supporting sustainable pollution mitigation. The FOMAC nanocomposites were prepared via synergistic coprecipitation, chemical activation, and sonication methods. The prepared nanocomposites were characterized by XRD, FTIR, SEM-EDX, VSM, BET, AAS, and well diffusion. The data analysis showed that FOMAC possessed an inverse spinel cubic structure for Fe_3O_4 and a face-centered cubic structure for MgO with crystallite sizes of 12.85 nm and 36.06 nm, respectively. FOMAC was confirmed to have spherical and chunk morphology with nanometric average particle sizes. The functional groups of Fe-O (octahedral and tetrahedral sites), Mg-O, and C═C were identified at wavenumbers of 452, 682, 804, and 1399 cm^{-1}, respectively. FOMAC had a high specific surface area of 30.6802 m^2/g and exhibited superparamagnetic properties with a saturation magnetization of 10.006 emu/g. Interestingly, FOMAC exhibits excellent performance against *E. coli* and *S. aureus* bacteria, with inhibition zone diameters of 12.49 mm and 14.10 mm, respectively. Moreover, FOMAC has an adsorption efficiency of 63.40% for Pb(II) removal. Interestingly, FOMAC had an adsorption efficiency up to 98.83% for Cd(II) removal. Thus, these findings indicate that FOMAC provides a scalable and sustainable materials strategy for environmental remediation, thereby improving environmental quality and reducing health risks to society from microbial and heavy metal (Pb(II) and Cd(II)) contamination.

1. Introduction

Clean water plays an essential role in maintaining ecosystem balance and supporting life. However, increasing dye, mining, metal electroplating, pharmaceutical, and battery industries have increased pollution from toxic heavy metals in water. The rapid growth of industry in recent years has caused major problems for human life, especially concerning aquatic environmental issues [1]. Various industries, such as paint, dye, textile, plastic, metal plating, and battery industries, generate large amounts of waste [2,3]. In general, industrial waste contains various heavy metal ions, dyes, and other hazardous substances that can threaten human health, even at low concentrations. Among these contaminants, the most dangerous are heavy metal wastes, such as Pb, Cd, Hg, As, Cu, Cr, Co, Zn, and Ni [4,5]. Worse, research data show that heavy metals have contaminated approximately 40% of rivers and lakes [6]. Theoretically, in water, heavy

Peer review under the responsibility of Editorial Board of Environmental Pollution and Management.
* Corresponding author.
E-mail address: ahmad.taufiq.fmipa@um.ac.id (A. Taufiq).

https://doi.org/10.1016/j.epm.2026.03.007
Received 29 October 2025; Received in revised form 30 January 2026; Accepted 17 March 2026
Available online 18 March 2026
2950-3051/© 2026 The Authors. Publishing services by Elsevier B.V. on behalf of KeAi Communications Co. Ltd. This is an open access article under the CC BY-NC-ND license (http://creativecommons.org/licenses/by-nc-nd/4.0/).

metals are materials that cannot be biodegraded, so they can accumulate throughout the food chain (bioaccumulation) and trigger serious health issues in living things, especially humans [7].

Among heavy metals, cadmium (Cd(II)) and lead (Pb(II)) are the most dangerous due to their high toxicity. According to a 2022 report by the World Health Organization (WHO), there were more than one million deaths and 21.7 million people worldwide suffering from disabilities due to consuming water exposed to Pb(II), and around 600 million people annually suffer from environmental pollution contaminated with Cd(II) [7–9]. Excessive Pb(II) and Cd(II) concentrations in water sources and in living organisms such as fish and shellfish are dangerous for humans to consume. Moreover, prolonged exposure to Pb (II) and Cd(II) causes various diseases, such as cardiovascular disorders, kidney failure, heart problems, intestinal problems, liver cirrhosis, brain damage, mental retardation, anemia, cancer, chronic lung disease, high blood pressure, leukemia, and genetic toxicity [7,9,10].

In addition to heavy metal exposure, contamination by pathogenic bacteria in aquatic environments is a serious environmental issue that requires serious attention from multiple stakeholders. Previous research has shown that dangerous contaminating bacteria such as *E. coli* and *S. aureus* are often found in drinking water. Moreover, contamination of drinking water with such bacteria can cause infections that affect the digestive tract, bloodstream, skin, and other organs [11]. If this issue remains unaddressed, it will have serious consequences for the sustainability of aquatic environments and public health.

Various strategies were employed for removing heavy metals and pathogenic bacteria from aquatic environments have been explored, including chemical precipitation, neutralization, ion flotation, ion exchange, coagulation, membrane separation, electrochemistry, and photocatalysis [12–15]. Nevertheless, these methods still have restraints, such as high production of toxic sludge that requires further processing, high costs, low efficiency, long processing times, and high energy requirements [16]. Meanwhile, current popular methods for water decontamination, such as photocatalysis, also still have limitations related to photo-carrier segregation, photocatalytic activity, effectiveness, and efficiency [17]. To reduce harmful bacterial contamination, several substances are often used in drinking water treatment, such as ozone, free chlorine, iodine, and chloramine. However, these substances tend to react with natural organic matter and other constituents in water, causing the formation of disinfection by-products and raising significant concerns [18]. Consequently, it is crucial to develop easier, simpler, faster, more efficient, and environmentally friendly methods to simultaneously remove heavy metals and bacteria from water, such as adsorption.

In recent years, the adsorption method has emerged as an alternative strategy for degrading or removing heavy metals from water because it is relatively inexpensive, energy efficient, effective, and environmentally friendly [19]. In this context, activated carbon (AC) is frequently used because it is abundant and easy to obtain in nature. In this work, AC obtained from sustainable biomass sources, such as coconut shells, has the advantage of being low-cost and environmentally friendly compared with AC derived from non-renewable sources, including coal [20,21]. AC from coconut shells has the additional advantage of a large specific surface area, pore volume, and abundant surface functional groups, making it potentially useful as an adsorbent [22]. In addition, coconut shells also contain phenolic compounds and acetic acid, which act as the main antimicrobial agents [23]. Despite its advantages, AC still has limitations, particularly the difficulty in separating from the solution after the adsorption process is complete [24]. This issue can be solved by incorporating AC with magnetic materials, such as Fe_3O_4.

Fe_3O_4 has been considered as excellent material with various unique properties, such as low toxicity, biodegradability, excellent catalytic activity and biocompatibility, high saturation magnetization, and superparamagnetic behavior [25]. So far, Fe_3O_4 is often synthesized using commercial chemical precursors such as hexahydrate ($FeCl_3.6H_2O$) and tetrahydrate of iron chloride ($FeCl_2.4H_2O$) [26]. Despite this, Fe_3O_4 can also be synthesized from natural materials such as iron sand at a lower cost, be more environmentally friendly, and exhibit high saturation magnetization [27]. Due to its unique properties, Fe_3O_4, prepared from iron with excellent magnetic properties, can be incorporated with AC to increase heavy metal adsorption and facilitate the separation of adsorbents from solutions using an external magnetic field [28]. Meanwhile, another advantage as an antibacterial agent, Fe_3O_4 can also produce reactive oxygen species on the surface of nanoparticles, resulting in oxidative stress in bacterial cells and culminating in cell death [29]. Despite its advantageous magnetic properties, Fe_3O_4 is easily oxidized, which leads to a reduction in magnetization [30]. Consequently, the incorporation of a secondary material, such as MgO, is required to inhibit Fe_3O_4 oxidation and enhance its chemical stability [31].

MgO is a stable metal oxide and can inhibit the oxidation of Fe_3O_4 by forming a barrier layer for oxygen diffusion to the surface of Fe_3O_4 [32]. In addition, MgO also has an advantage due to its low toxicity [33]. In heavy metal adsorption applications, MgO is desirable because it has many adsorption sites, so it can also increase the adsorption capacity of AC [34]. Moreover, as an antibacterial agent, MgO can form superoxide radicals through the reaction of oxygen with the bacterial surface. These extra electrons are highly reactive and can damage proteins and phospholipids of bacterial membranes [35]. Therefore, incorporating them into Fe_3O_4/MgO/AC (FOMAC) nanocomposites as bifunctional materials is important for environmental remediation.

Previous research conducted by Hanif *et al.* showed that adsorption efficiency was achieved up to 98% for the removal of Cd(II) within 15 min using Ag/MgO@Fe_3O_4 [36]. However, at a low concentration of 0.06 ppm, the study did not provide the adsorption capacity. Such research showed that Fe_3O_4 was not synthesized from natural materials without conducting antibacterial applications. Furthermore, Esmaeili *et al.* reported the adsorption efficiency of 96.65% for the removal of As (III) using Fe_3O_4@MgO@AC. However, it required a longer time of 35 min, a low capacity of only 1.166 mg/g. Such research also showed that Fe_3O_4 was not synthesized from natural materials without conducting antibacterial applications [37]. Zadeh et al. reported that the use of AC/alginate/Fe_3O_4 had good adsorption performance on Pb(II) with an adsorption efficiency of 97.83% and an adsorption capacity of 37.764 mg/g [38]. However, according to the report by Aydin et al., alginate did not exhibit any inhibitory effect on bacteria [39]. On the other hand, Fekri et al. reported that AC/Fe_3O_4 has a cefazolin adsorption capacity of up to 96% and good antibacterial properties [40]. Meanwhile, Anigol et al. also reported that Fe_3O_4-MgO also has excellent antibacterial activities against various strain bacteria [41]. However, in the two recent studies, Fe_3O_4 was still synthesized from commercial chemicals and not from natural materials. Therefore, in this research, the synthesis of Fe_3O_4/MgO/AC (FOMAC) nanocomposites was carried out by employing iron sand and coconut shell as adsorbents for heavy metals Cd(II) and Pb(II) for environmental remediation, especially in water. In addition, the nanocomposites also open the potential as antibacterial agents that can help reduce microbial contamination in water, such as *S. aureus* and *E. coli*.

2. Experimental Methods

2.1. Materials

The natural materials used in this research included iron sand, which was achieved from Sine Beach, Indonesia, and coconut shell, which was obtained from farmers' gardens in Jember Regency, East Java, Indonesia. The reagents employed in the synthesis process were magnesium oxide (MgO, ≥98%, Smartlab, Indonesia), deionized water (≥99.9%, Onelab waterone, Indonesia), hydrochloric acid fuming (HCl 37% 2 M, Merck, Germany), ammonia solution (NH_4OH 25% 6.5 M, Merck, Darmstadt, Germany), nitrid acid (HNO_3 65% 2 M, Smartlab,

Indonesia), ammonia (NH_3 25% 2 M, Smartlab, Indonesia), ethanol (70%, Smartlab, Indonesia), alcohol (70%, Smartlab, Indonesia), distilled water (≥99.9%, Hydrobatt, Indonesia), dimethyl sulfoxide (DMSO ≥99.9%, Merck, Germany), lead (II) nitrate ($Pb(NO_3)_2$, ≥ 99.95%, Smartlab, Indonesia), and cadmium nitrate tetrahydrate ($Cd(NO_3)_2.4H_2O$, ≥ 98%, Merck, Germany).

2.2. Synthesis of Fe_3O_4 Nanoparticles from Iron Sand

A total of 20 g of natural iron sand resulting from the separation was reacted with HCl using a hot plate and magnetic stirrer with a stirring speed of 720 rpm, then filtered to obtain a $FeCl_2$ and $FeCl_3$ solutions. A total of 18 mL of solutions was then titrated with 25 mL of NH_4OH for 30 min and stirred until a black precipitate formed. The precipitate was washed with H_2O until the pH was neutral, then filtered and dried in an oven at 100 °C for 1 h until pure Fe_3O_4 powder was obtained [42]. The Fe_3O_4 powder was then crushed with a mortar to obtain Fe_3O_4 nanoparticles.

2.3. Synthesis of AC Derived from Coconut Shell

A total of 1000 g of coconut shell was cleaned, dried, and burned until it became charcoal. The charcoal was then crushed and sifted to obtain powdered product. The powdered charcoal was then heated at 600 °C for 2 h, then crushed using a mortar and pestle [22]. A total of 10 g of charcoal was dissolved in 100 mL of HNO_3 at a temperature of 80 °C for 2 h until a black precipitate formed. The precipitate was washed with ethanol until the pH was 5 or 6, then placed in the oven at 100 °C for 1 h until the AC powder was obtained, followed by a crushing process.

2.4. Synthesis of Fe_3O_4/MgO/AC (FOMAC) Nanocomposites

The prepared Fe_3O_4 (1 g) was dispersed and stirred at 80 °C for 30 min in 80 mL of distilled water until homogeneous. After that, 1 g of MgO and 0.15 g of AC were added to the solution, then sonicated for 30 min. The solution was then stirred and titrated with 7.5 mL of NH_3 for 1 h at 80 °C. After the reaction was complete, the solution was precipitated using a magnet and washed to obtain a neutral pH, then dried in an oven at 100 °C for 1 h until Fe_3O_4/MgO/AC (FOMAC) powder was obtained.

2.5. Characterization

XRD characterization was carried out with instrument specifications PANalytical type X'Pert PRO to determine the crystal structure, lattice parameters, and crystallite size; SEM-EDX (FEI type Inspect-S50) was employed to evaluate the morphology, particle size, and elemental content; FTIR with instrument specifications Shimadzu type IR-Prestige21 to characterize chemical functional groups; VSM instrument specifications with Quantum Design PPMS® VersaLab™ to characterize magnetic properties; SAA-BET with instrument specifications Micromeritics Tristas II Plus to determine the specific surface area AAS with instrument specifications Shimadzu AA 7800 to determine the effectiveness of FOMAC nanocomposites in adsorbing heavy metals Pb (II) and Cd(II); and antibacterial test using DMSO to determine the bacterial inhibition of the nanocomposites. Furthermore, for adsorption test, a total of 0.160 g of $Pb(NO_3)_2$ and 0.274 g of $Cd(NO_3)_2.4H_2O$ were each dissolved in 100 mL of DI water to form a stock solution of 1000 ppm heavy metal contamination. A total of 10 mL of the stock solution was dissolved in 90 mL of DI water to obtain a 100 ppm solution. Next, the solution was reacted with Fe_3O_4/MgO/AC (FOMAC) based on variations in contact time, temperature, concentration, and pH.

2.6. Data Analysis

2.6.1. Adsorption Capacity and Efficiency

Adsorption capacity and efficiency are calculated using Eq. (1) and (2).

$$q_t = \frac{(C_0 - C_t)}{m} \times V \tag{1}$$

$$\%\text{adsorption} = \frac{(C_0 - C_t)}{C_0} \times 100\% \tag{2}$$

Where q_t is the adsorption capacity (mg/g), C_0 is the initial concentration (mg/L), C_t is the final concentration (mg/L), V is the volume of heavy metal solution (L), and m is the adsorbent mass (g) [19,43].

2.6.2. Adsorption Kinetics

The adsorption kinetics of the pseudo-first order method (first order linear regression) Lagergren model is shown by Eq. (3).

$$\log(q_e - q_t) = \log q_e - \frac{k_1}{2.303} t \tag{3}$$

The pseudo-second order McKay & Ho model is shown in Eq. (4).

$$\frac{t}{q_t} = \frac{1}{k_1 q_e^2} + \frac{1}{q_e} t \tag{4}$$

Apart from that, the intra-particle diffusion model is shown by Eq. (5)

$$q_t = k_i\left(t^{\frac{1}{2}}\right) + C \tag{5}$$

Where q_e represents equilibrium adsorption capacity (mg/g), k_1 represents first order rate constant (min^{-1}), k_2 represents second order rate constant ($g/mg.min^{-1}$), t represents time (min), k_i represents average rate constant ($g/mg.min^{-1/2}$), and C represents heavy metal concentration (mg/g). Based on Eq. (3), a graph of the relationship between log ($q_e - q_t$) and t is obtained. Meanwhile, from Eq. (4), a graph of the relationship between t/q_t and t is obtained [43].

2.6.3. Adsorption Thermodynamics

Adsorption thermodynamic analysis uses Eqs. (6), (7), and (8).

$$K_C = \frac{C_0}{C_e} \tag{6}$$

$$\Delta G^\circ = -RT \ln K_C \tag{7}$$

$$\ln K_C = \frac{-\Delta H^\circ}{RT} + \frac{\Delta S^\circ}{R} \tag{8}$$

Where K_C is the equilibrium constant, C_0 is the initial adsorbate concentration, C_e is the adsorbate concentration at equilibrium, R is the ideal gas constant (8.314 J/mol.K), and T is the temperature (K). The ΔG° value is obtained from the ln K_C value, while the ΔH° and ΔS° values are obtained from the Van't Hoff curve through the relationship between ln K_C and $1/T$ [37].

2.6.4. Adsorption Isotherm

The Langmuir Isotherm is shown by Eqs. (9) and (10).

$$q_e = \frac{Q_0 b_L C_e}{(1 + b_L C_e)} \tag{9}$$

$$\frac{C_e}{q_e} = \frac{1}{Q_0 b_L} + \frac{C_e}{Q_0} \tag{10}$$

Where q_e represents equilibrium adsorption capacity (mg/g), C_e represents equilibrium concentration of adsorbate (mg/L), b_L represents Langmuir constant (L/mg), and Q_0 represents Langmuir adsorption capacity (mg/g). From this equation, a graph of the relationship between C_e/q_e and C_e can be obtained to find the adsorption capacity (Q_0)

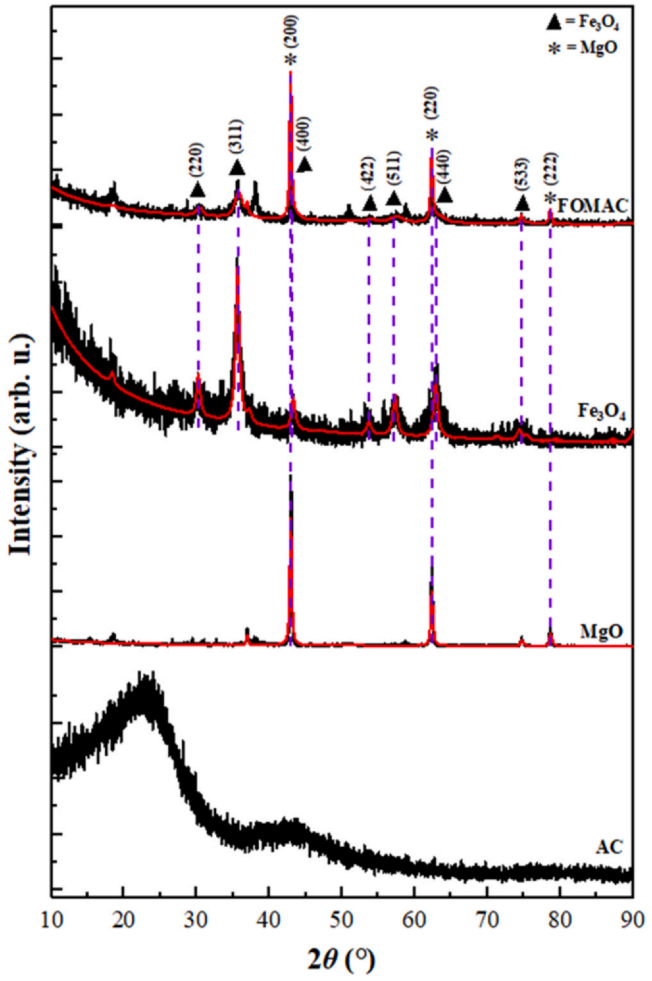

Fig. 1. XRD patterns of Fe_3O_4, MgO, AC, and FOMAC.

and Langmuir constant (b_L). Meanwhile, the Freundlich isotherm is shown by Eqs. (11) and (12).

$$q_e = K_f C_e^{\frac{1}{n}} \tag{11}$$

$$\log q_e = \log K_f + \frac{1}{n} \log C_e \tag{12}$$

Where K_f and n are the physical constants of the Freundlich isotherm, which can be obtained from the relationship graph between log q_e and log C_e. The appropriate adsorption isotherm model can be determined from the level of linearity of the line, which is characterized by an R^2 value close to one [37,43].

3. Results and Discussion

3.1. Crystal Structure of FOMAC Nanocomposites

The XRD pattern of FOMAC nanocomposites is shown in Fig. 1, showing the conformity of the experimental results with the Fe_3O_4 (AMCSD 0007423) and MgO (AMCSD 1000053) databases. The black line shows the experimental data, while the red line shows the refinement results. The success of FOMAC synthesis is marked by the identification of typical diffraction peaks of Fe_3O_4 and MgO nanoparticles. The Fe_3O_4 diffraction peaks were detected at 2θ = 30.28°; 35.66°; 43.35°; 53.78°; 57.34°; 62.97°, and 74.52° with the hkl planes (220), (311), (400), (422), (511), (440), and (533). Meanwhile, MgO nanoparticles were identified at 2θ = 42.96°; 62.52°; 78.69° with hkl planes (200), (220), and (222) [44]. The crystal structures of Fe_3O_4 and MgO

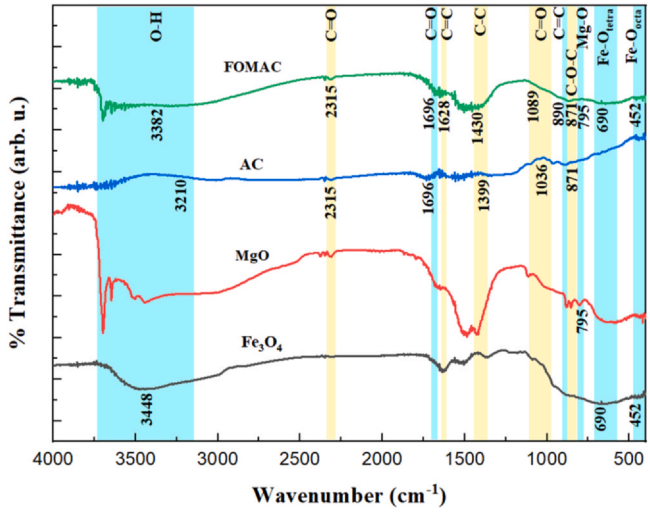

Fig. 2. FTIR spectra of Fe_3O_4, MgO, AC, and FOMAC.

were in accordance with previous research, where Fe_3O_4 had an inverse cubic spinel structure with a space group of *Fd-3m* and MgO had a face-centered cubic structure with A space group of *Fm-3m* [45,46]. Meanwhile, the AC diffraction peaks were not identified because it has an amorphous (non-crystalline) structure. Based on quantitative analysis, the Fe_3O_4 and MgO have crystallite sizes of 15.76 nm and 36.06 nm, respectively. Meanwhile, the crystallite size of MgO remains at 36.06 nm, but specifically, the Fe_3O_4 phase decreases to 12.85 nm because there is a role of AC, which reduces the crystallite size. Furthermore, the lattice parameter of pure Fe_3O_4 is 8.3598 Å and pure MgO is 4.2132 Å, while in FOMAC, there is a decrease in the lattice parameter, namely 8.3236 Å for Fe_3O_4 and 4.2098 Å for MgO. This occurs because of the increase in internal pressure in FOMAC so that the lattice parameter value decreases [47]. The identification of the nano-sized crystal structure indicates that FOMAC has been successfully synthesized. The nano-scale crystal structure also provides more active sites, thereby increasing the adsorption capacity for heavy metals Pb(II) and Cd(II) [19].

3.2. Functional Groups of FOMAC Nanocomposites

Fig. 2 shows the FTIR spectrum analysis of Fe_3O_4, MgO, AC, and FOMAC. In the Fe_3O_4 and FOMAC structures, Fe–O (tetrahedral and octahedral) bonds are identified at wavenumbers of 452 and 690 cm^{-1}, respectively [42]. The results of FTIR analysis for AC, vibrations of C═C, C–C, and C–O appear at 2315, 1399, and 1036 cm^{-1}, respectively. While in FOMAC, the C═C bond is detected at 2315, 1628, and 890 cm^{-1}, and the C–C and C–O bonds at 1430 and 1089 cm^{-1}, respectively [37]. In addition, in AC and FOMAC, there are peaks at 1696 cm^{-1} from C═O vibrations and at 871 cm^{-1} from C–O–C stretching vibrations of carbonyl compounds such as esters [48]. In MgO and FOMAC, Mg–O bonds are also identified at 795 cm^{-1}. The broad peaks of O–H bonds belonging to Fe_3O_4, AC, and FOMAC are detected at 3448, 3210, and 3382 cm^{-1} [37]. The emergence of all functional group bonds indicates that the synthesis of Fe_3O_4, AC, and FOMAC was successful. In addition, the O–H and C═O group bonds also play a role in adsorption because they can form ionic bonds or coordinate with heavy metals Pb(II) and Cd(II) [49].

3.3. Morphology, Particle Size, and Elemental Composition of FOMAC Nanocomposites

The success of the synthesis process is also confirmed through the EDX results, as shown in Table 1. The constituent elements of FOMAC, such as Fe, O, Mg, and C appear. The morphology and particle size

Table 1
Elemental composition of Fe_3O_4 and FOMAC.

Sample	Elemental composition			
	Fe	O	Mg	C
Fe_3O_4	70%	30%	–	–
FOMAC	40%	38.3%	11.2%	10.5%

distribution resulting from SEM characterization of Fe_3O_4, AC, and FOMAC are shown in Fig. 3.

In this work, Fe_3O_4 forms spherical and AC forms like chunks. Meanwhile, the morphology of FOMAC looks like a combination of spheres and chunks. Based on the results of quantitative analysis, it is known that the average spherical particle size is confirmed as nanoscale, namely 30.03 nm for pure Fe_3O_4 and 20.75 nm in FOMAC [42]. The smaller the particle size, the higher the surface area of the adsorbent, which can increase the adsorption capacity of heavy metals Pb(II) and Cd(II). Meanwhile, AC is confirmed to have an average pore diameter of 45.64 nm, which allows heavy metals to diffuse into it so that adsorption of Pb(II) and Cd(II) can take place optimally [43].

3.4. Magnetic Properties of FOMAC Nanocomposites

The magnetic properties of Fe_3O_4 and FOMAC, characterized by VSM at room temperature, are shown in Fig. 4. The characterization results were analyzed using the Langevin method based on Eqs. (13) and (14).

$$M = M_r + M_s\left(\coth(C\times H) - \frac{1}{C\times H}\right) + \mu \times H \tag{13}$$

$$C = \frac{\mu}{k_B T} \tag{14}$$

Where M represents magnetization (emu/g), M_s represents saturation magnetization (emu/g), M_r represents remanent magnetization (emu/g), χ represents susceptibility, μ represents magnetic moment, H represents magnetic field with unit (Oe), T represents temperature, and k_B represents Boltzmann's constant (1.38×10^{-23} J/K) [50,51]. The analyzed results are depicted in Table 2.

Qualitatively, Fe_3O_4 and FOMAC have superparamagnetic properties as evidenced by the S-shaped hysteresis curve with small saturation magnetization (M_s) values of 24.118 emu/g for Fe_3O_4 and 10.006 emu/g for FOMAC. After incorporation, the magnetization value of FOMAC

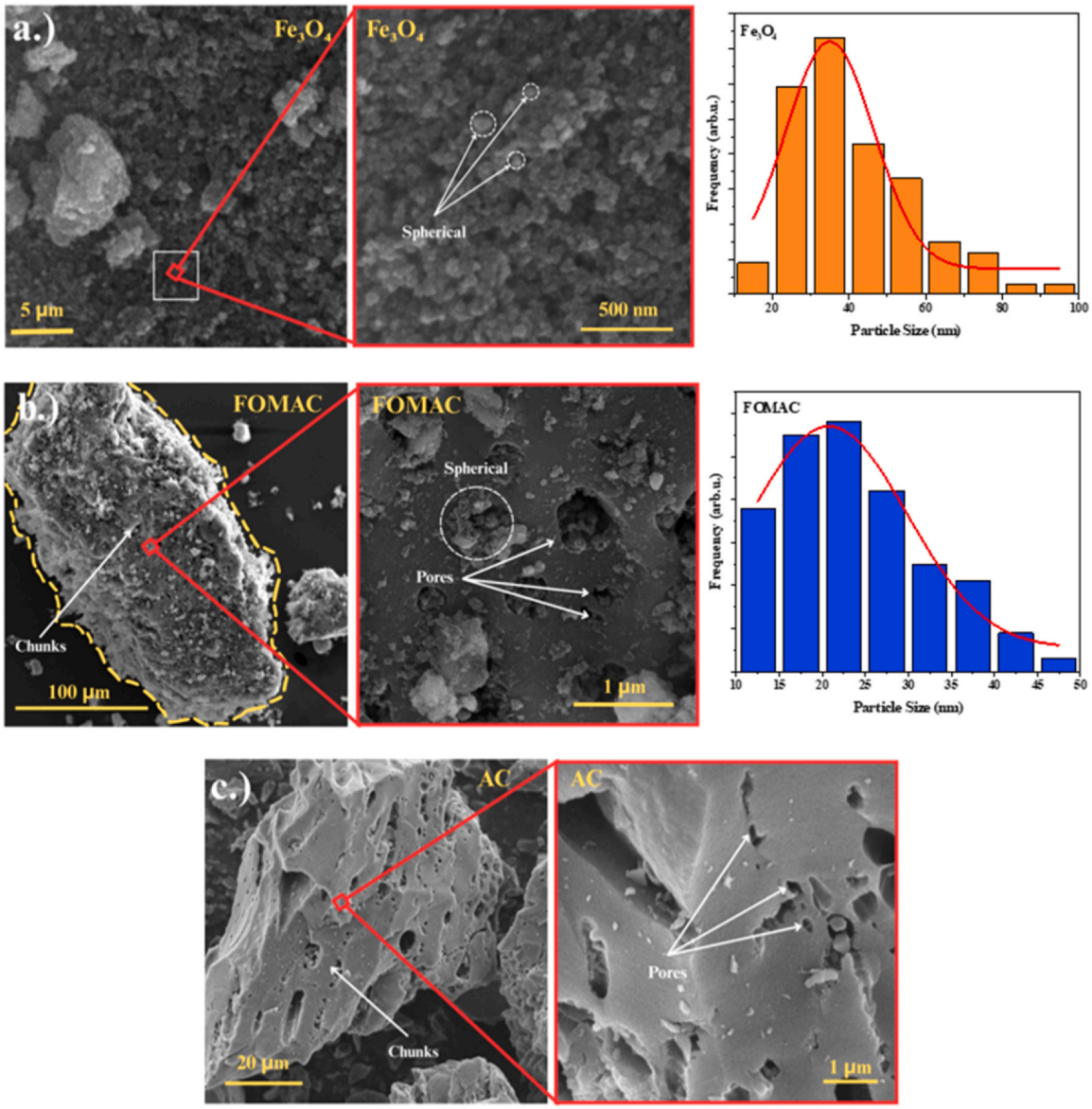

Fig. 3. Morphology and particle size distribution of (a) Fe_3O_4, (b) FOMAC, and (c) morphology of AC.

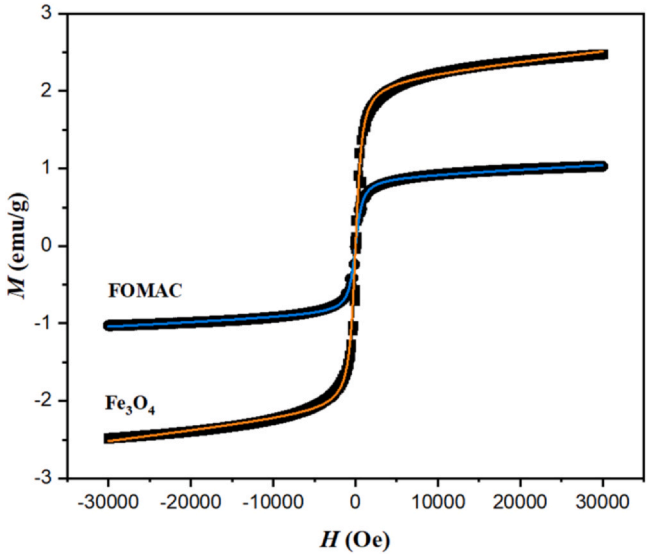

Fig. 4. Hysteresis curves of Fe_3O_4 and FOMAC.

Table 2
Magnetic properties of (a) Fe_3O_4 (b) FOMAC.

Sample	M_s (emu/g)	M_r (emu/g)	H_c (Oe)	χ (10^{-4})
Fe_3O_4	24.118 ± 0.004	0.022 ± 0.015	88.270 ± 0.005	1.284 ± 0.022
FOMAC	10.006 ± 0.017	0.013 ± 0.005	73.277 ± 0.005	0.549 ± 0.008

is smaller than that of Fe_3O_4, which is caused by the presence of MgO and AC as diamagnetic materials. In addition, factors such as particle size and shape, crystal structure, and interactions with the matrix greatly influence the magnetic behavior of the synthesized samples [52]. However, FOMAC still has strong magnetic properties, enabling easy separation from the suspension using a magnet. Apart from that, the magnetic properties of FOMAC also play a role in attracting heavy metals such as Pb(II) and Cd(II) in the adsorption process, so that the adsorption capacity increases [37]. The remanent magnetization (M_r) and susceptibility (χ) values can be ignored because they have values close to zero. In addition, the field coercivity (H_c) has a value close to zero Tesla (1 Tesla = 10,000 Oe), so it can also be ignored [53].

3.5. Specific Surface Area of FOMAC Nanocomposites

The Brunauer–Emmett–Teller (BET) method has been used in nanomaterial characterization for the past few decades because it is considered the best method for determining the surface area of materials. The specific surface area of FOMAC can be calculated by plotting a graph of the relationship between $1/[Q(P/P_0)-1]$ vs P/P_0 (Fig. 5) [54]. The graph is linear, as evidenced by the value of $R^2 = 0.9999$, and the slope is $y = 0.1399x + 0.0021$. The results obtained a specific surface area of FOMAC of 30.6802 m^2/g. The surface area of FOMAC is larger than that of the previous study, which stated the surface area of Fe_3O_4 composite AC of 12.04 m^2/g [55]. A large specific surface area of materials can provide more active sites so as to increase the heavy metal adsorption capacity [56,57].

3.6. Antibacterial Activity of FOMAC Nanocomposites

The FOMAC nanocomposites exhibit excellent antibacterial activity against *E. coli* and *S. aureus* bacteria. FOMAC was able to inhibit *E. coli* and *S. aureus* bacteria with inhibition zone diameters of (12.49 ± 0.48) mm and (14.10 ± 1.56) mm, respectively. Based on

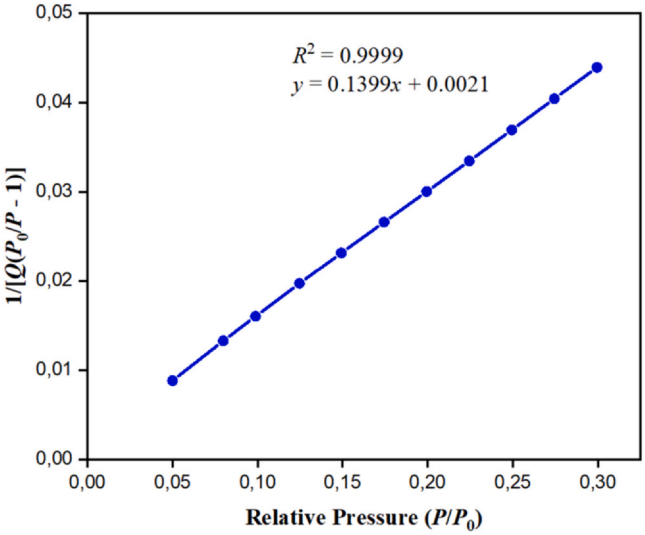

Fig. 5. A plot of $1/[1/[Q(P/P_0)-1]$ vs P/P_0.

the classification of inhibitory responses by the Clinical and Laboratory Standard Institute (CLSI) [58], this result is classified as resistant. Theoretically, FOMAC is able to inhibit bacterial growth due to the electrostatic forces that occur between the nanocomposite and bacteria. As a result, reactive oxygen species (ROS) are generated, which limit amino acid synthesis and DNA replication, thereby damaging the core and pathogenic DNA [59]. The antibacterial mechanism of FOMAC is shown in Fig. 6.

3.7. Adsorption Performance of FOMAC Nanocomposites on Pb(II) and Cd (II)

3.7.1. Effect of Contact Time and Adsorption Kinetics Model

The performance of FOMAC in adsorbing Pb(II) and Cd(II) was measured in the time range between 5 and 30 min by controlling the temperature at 27 °C, initial concentration of 100 ppm, and pH 5 (Fig. 7). The graph shows that as the contact time increases, the adsorption capacity of FOMAC also increases. Adsorption occurs in two

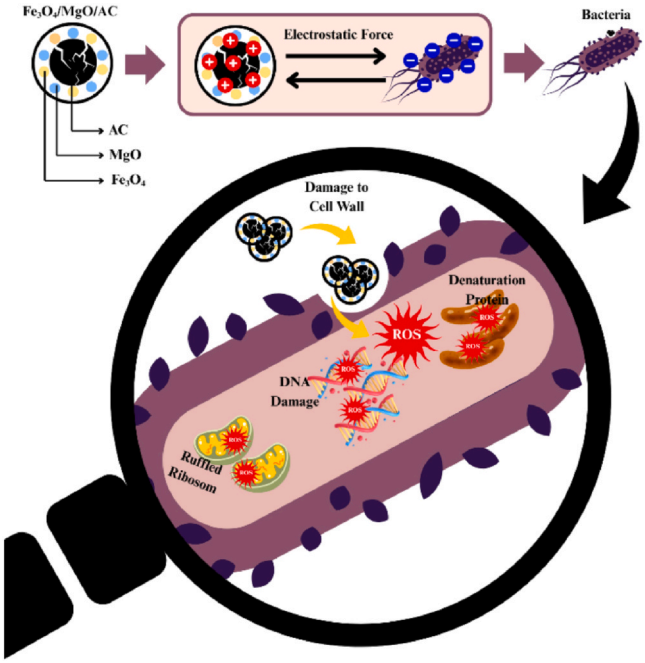

Fig. 6. Antibacterial mechanism of FOMAC.

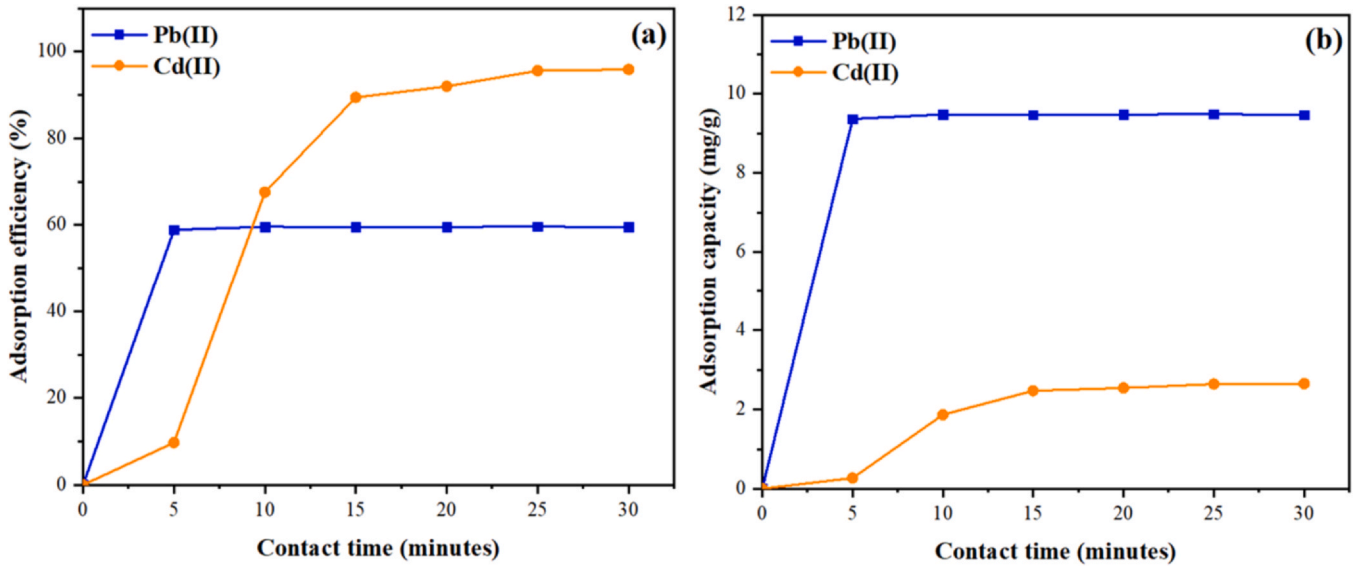

Fig. 7. (a) Efficiency and (b) capacity of adsorption of Pb(II) and Cd(II) by FOMAC with adsorption conditions of temperature 27 °C, solution concentration 100 ppm, and pH 5.

stages. In the first stage, the adsorption rate is quite fast due to the availability of many active sites, functional groups, and pores on the surface of the adsorbent as reported by previous works [43,60]. In the second stage, adsorption increases more slowly because the active sites are saturated with increasing contact time. FOMAC reaches equilibrium after 25 min for Pb(II) with an efficiency of 59.64% and an adsorption capacity of 9.587 mg/g. Meanwhile, FOMAC reaches equilibrium after 30 min for Cd(II) with an efficiency of 95.91% and an adsorption capacity of 2.651 mg/g. From the results of the effect of contact time, adsorption kinetics analysis can be carried out, and the results can be seen in Table 3.

The adsorption rate of Pb(II) and Cd(II) from water is very important in treatment processes. This rate determines the efficiency of FOMAC as a heavy metal adsorbent in water treatment. The pseudo-second order model is more suitable for the adsorption of Pb(II), and the pseudo-first-order model is more suitable for the adsorption of Cd (II) by FOMAC, as evidenced by the R^2 value, which is close to or equal to 1. These results also indicate that the intraparticle diffusion model is not suitable [43].

3.7.2. Effect of Temperature and Adsorption Thermodynamics Model

In this work, adsorption experiments were carried out at a temperature range of 25–40 °C (298–313 K) to measure the effect of temperature on the adsorption of Pb(II) and Cd(II) by FOMAC by controlling the contact time of 15 min, initial concentration of 100 ppm, and pH 5. In general, there is an increase in the adsorption of Pb(II) and Cd (II) as the adsorption temperature increases, as shown in Fig. 8. This means that the adsorption process occurs endothermically. This can happen because the Pb(II) and Cd(II) ions gain enough energy as the temperature increases, thus increasing their mobility to interact with the active sites on the surface of the FOMAC adsorbent. The similar adsorption trends of Pb(II) and Cd(II) indicate that both are adsorbed at the same site with electrostatic interactions, identical hydrogen bonds, or π–π interactions; therefore, they exhibited diverse adsorption performances [61]. Moreover, the best efficiency performance for Pb(II) for temperature variation measurement was 63.40% with an adsorption capacity of 11.121 mg/g at a temperature of 40 °C (313 K). Meanwhile, for Cd(II), the best results were obtained with an efficiency of 95.84% and an adsorption capacity of 2.740 mg/g. From the results of the effect of this temperature, thermodynamic analysis of adsorption can be carried out, and the results can be seen in Table 4.

The spontaneity and feasibility of Pb(II) and Cd(II) adsorption by FOMAC can be determined using thermodynamic parameters, as shown in Table 4. The parameters evaluated at different temperatures indicate an endothermic reaction as evidenced by the positive ΔH° values for all adsorbents. In general, endothermic reactions enhance the adsorption of pollutants such as heavy metals with increasing temperature. The ΔS° values are also positive, indicating the increasing randomness and degrees of freedom of Pb(II) and Cd(II) in solution. The adsorption of Pb (II) and Cd(II) by FOMAC can occur spontaneously as implied by the negative ΔG° values [37,43].

Table 3
Results of the adsorption kinetics model analysis.

Adsorption kinetic model	Parameter	Heavy metals	
		Pb(II)	Cd(II)
Pseudo-first order	q_e (mg/g)	1.712	2.702
	k_1 (min^{-1})	-3.47×10^{-4}	–0.014
	R^2	0.356	0.832
Pseudo-second order	q_e (mg/g)	9.488	3.263
	k_2 (g.mg/min)	3.584	7.83×10^3
	R^2	1.000	0.982
Intra-particle diffusion	C (mg/g)	9.354	1.057
	k_i ($g/g.min^{1/2}$)	0.026	0.314
	R^2	0.468	0.775
Experimental	q_e (mg/g)	11.121	3.053

3.7.3. Effect of Initial Concentration and Adsorption Isotherm Models

The initial concentration effect on the heavy metal adsorption was assessed in the range of 20–100 ppm by controlling the contact time of 15 min, temperature of 27 °C, and pH 5. The results are shown in the graphs in Fig. 9. Both graphs show an increase in the adsorption of Pb (II) and Cd(II) as the solution concentration increases. This phenomenon reveals that the heavy metal adsorption process depends on the concentration. This adsorbent behavior is also in line with previous work, which explains that the increase in adsorption capacity as the concentration of heavy metal solutions increases, associated with high mass transfer resistance [62]. Moreover, for high concentrations, such as 100 ppm, more interactions between the adsorbent surface and heavy metals Pb(II) and Cd(II) were considered. Therefore, at this concentration, the highest adsorption capacity was successfully observed. The results of measuring the effect of this initial concentration obtained the best results for Pb(II) with an efficiency of 59.53% and an

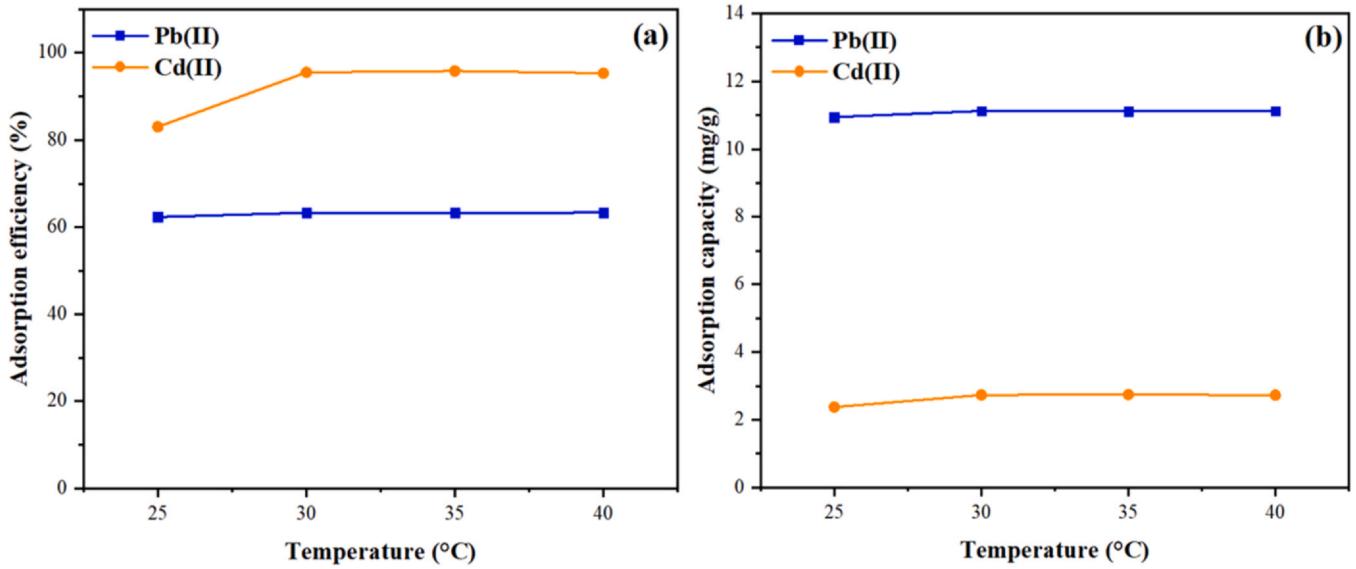

Fig. 8. (a) Efficiency and (b) capacity of adsorption of Pb(II) and Cd(II) by FOMAC with adsorption conditions of contact time 15 min, solution concentration 100 ppm, and pH 5.

Table 4
Results of the adsorption thermodynamic model analysis.

Temperature		Adsorption thermodynamic parameters					
		ΔH° (J/mol)		ΔS° (J/mol)		ΔG° (J/mol)	
˚C	K	Pb(II)	Cd(II)	Pb(II)	Cd(II)	Pb(II)	Cd(II)
25	298	18.209	894.503	0.180	15.302	–2.423	–4.394
30	303					–2.531	–7.825
35	308					–2.569	–8.140
40	313					–2.615	–7.983

adsorption capacity of 9.469 m/g. Meanwhile, for Cd(II) the best results were obtained with an efficiency of 93.97% and an adsorption capacity of 3.053 mg/g. From the results of the effect of this concentration, an adsorption isotherm analysis can be carried out, as shown in Table 5.

The maximum adsorption and interaction mechanisms of Pb(II) and Cd(II) by FOMAC can be calculated using the Langmuir and Freundlich isotherm analysis, assessed using the equilibrium data obtained at 27 ˚C (300 K). Table 5 shows that the Langmuir isotherm model is more appropriate for Cd(II) and the Freundlich isotherm for Pb(II). These results indicate that Cd(II) adsorption by FOMAC occurs at active sites on homogeneous surfaces in monolayer coverage, while Pb(II) adsorption by FOMAC occurs at active sites on heterogeneous surfaces [37,43].

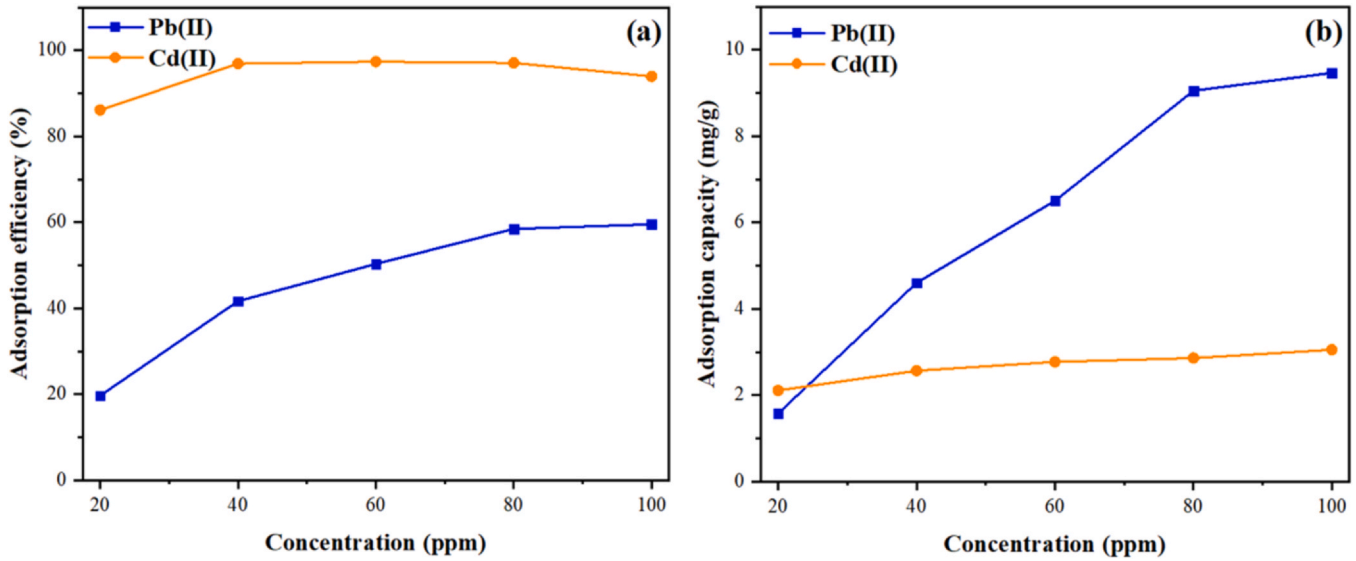

Fig. 9. (a) Efficiency and (b) capacity of adsorption of Pb(II) and Cd(II) by FOMAC with adsorption conditions of temperature 27 ˚C, contact time 15 min, and pH 5.

Table 5
Results of the adsorption isotherm model analysis.

Adsorption isotherm model	Parameter	Heavy metals	
		Pb(II)	Cd(II)
Langmuir	Q_0 (mg/g)	0.013	2.003
	b_L (L/mol)	0.078	17.960
	R^2	0.272	0.977
Freundlich	K_f	124.738	2.207
	n	0,771	–7.93
	R^2	0.037	0.365
Experimental	q_e (mg/g)	11.121	3.053

3.7.4. Effect of pH

The adsorption of Pb(II) and Cd(II) by FOMAC was evaluated at pH 3, 5, 7, 9, and 11 by controlling the contact time of 15 min, at a temperature of 27 °C, and an initial concentration of 100 ppm. The results are shown in Fig. 10. The adsorption capacity of FOMAC tends to be greater in basic solutions, which is the best result at pH 7 and 9 for Pb (II) and at pH 11 for Cd(II). This result is related to the presence of deprotonation of the adsorbent surface, resulting in increased electrostatic interactions and higher adsorption. At low pH (acidic), the adsorption of Pb(II) and Cd(II) tends to be minimal due to the weak electrostatic interactions caused by the functional groups on the adsorbent surface being protonated and acquiring a positive charge [43,63]. At pH 7 and 9, the efficiencies of the adsorbents for Pb(II) are 0.48% with an adsorption capacity of 0.031 mg/g. Interestingly, at pH 11, the efficiency of the adsorbents for Cd(II) wis 98.83% with an adsorption capacity of 2.831 mg/g. The efficiency and adsorption capacity for Pb(II) with pH variation were significantly lower compared to temperature, time, and concentration variations, due to the heavy metal solution being less homogeneous when acidified with HCl or when basicized with NaOH, so that the adsorbent absorbs both liquids and experiences saturation before absorbing Pb(II).

3.7.5. Adsorption Mechanism

The proposed adsorption mechanism for heavy metals Pb(II) and Cd (II) is shown in Fig. 11. The FTIR spectrum shows the presence of O-H, C-H, and C═O groups on the surface of the adsorbent for the adsorption of Pb(II) and Cd(II). Fe_3O_4 and MgO have high specific surface areas and surfaces rich in hydroxyl groups O-H which help in the adsorption of heavy metals [19]. Likewise, AC can absorb heavy metals Pb(II) and Cd(II) through highly active surface structure functional groups. Pb(II) and Cd(II) are heavy metals that are positively charged in aqueous solution [49]. At a low pH solution (acid), protons are widely available on the surface of the adsorbent, so that there is ionic repulsion during adsorption. Conversely, at high pH (base), the surface of the adsorbent becomes negatively charged so that its adsorption capacity is higher because there is no ionic repulsion between the heavy metal and the surface of the adsorbent [64]. At pH above 8, the C-OH bond on the surface becomes CO^-, thereby electrostatic attraction occurs between the positively charged heavy metal and the negatively charged adsorbent surface, so that the adsorption capacity will increase [43]. Based on the experimental results, the adsorption process follows the Langmuir isotherm, which shows that the adsorption mechanism is limited by the monolayer coverage. Furthermore, the thermodynamic results show that the adsorption process is spontaneous and endothermic [65].

3.7.6. Comparison Study

Tables 6 and 7 show the comparison of the adsorption capacity of FOMAC with several adsorbents. The tables exhibit adsorption capacity of FOMAC is one of the highest values reported. FOMAC, consisting of a combination of Fe_3O_4, MgO, and AC, is a promising agents for water purification with the advantages of high specific surface area, active functional groups that increase adsorption capacity, magnetic properties that facilitate separation from aqueous solutions, and cheap raw material prices. FOMAC has experimentally shown good adsorption performance at normal temperatures in several countries, including Indonesia. This is evidenced by the results of the test parameters of 25 min contact time, temperature 27 °C, initial concentration 100 ppm, and pH 5 for Pb(II), obtaining the efficiency and adsorption capacity 59.64% and 9.587 mg/g, respectively. However, for Pb(II), at the same pH and concentration, and at a temperature of 40 °C with a contact time of 15 min, the efficiency and adsorption capacity are 63.40% and 11.121 mg/g, respectively. Meanwhile, for a contact time of 15 min, a temperature of 27 °C, an initial concentration of 100 ppm, and a pH of 11, the highest efficiency and adsorption capacity are 93.97% and 3.053 mg/g, respectively. Based on these comparisons, it can be concluded that the FOMAC nanocomposites in this work exhibit superior adsorption performance than other adsorbents, positioning them as new bifunctional materials for environmental remediation.

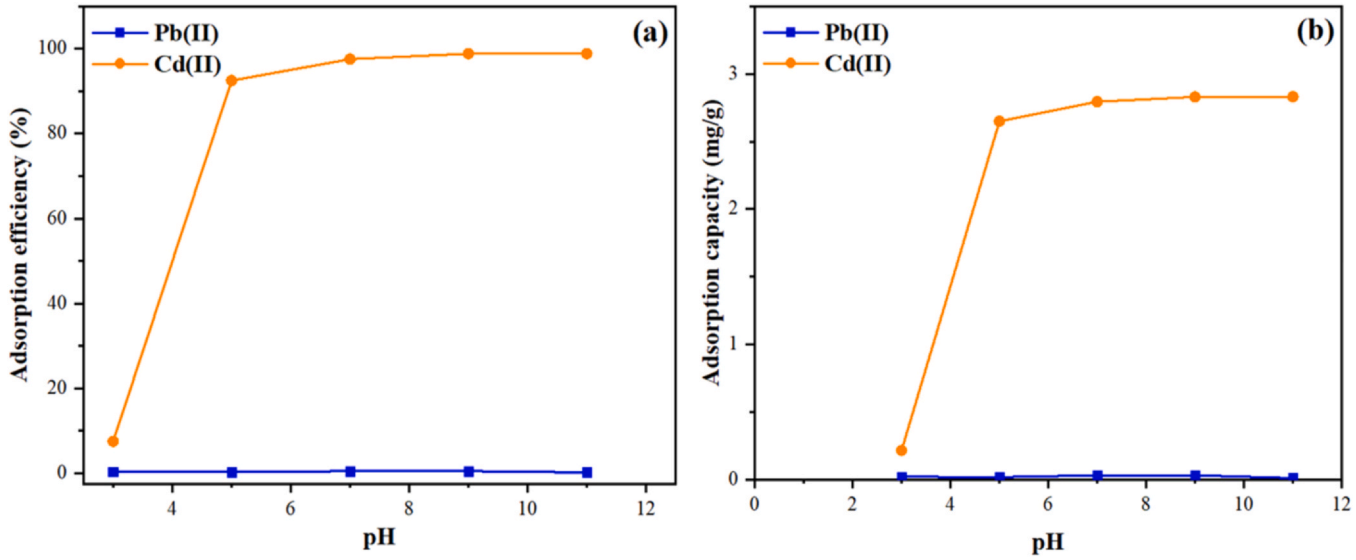

Fig. 10. (a) Efficiency and (b) capacity of adsorption of Pb(II) and Cd(II) by FOMAC with adsorption conditions of temperature 27 °C, contact time 15 min, and solution concentration 100 ppm.

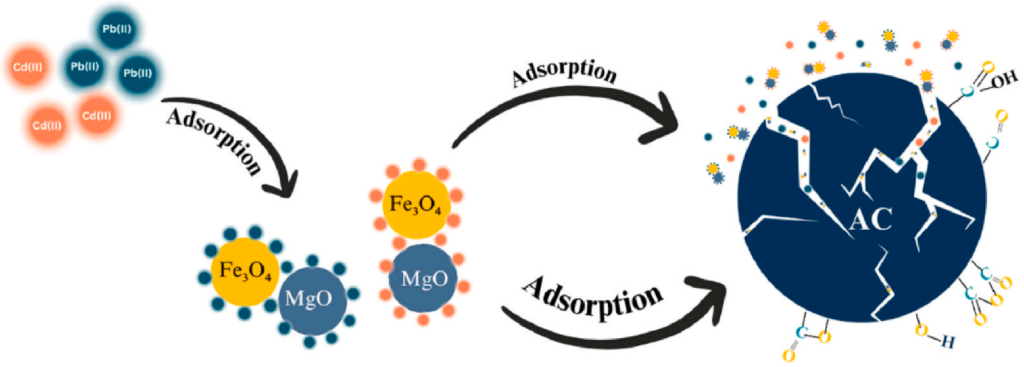

Fig. 11. Heavy metals adsorption mechanism of FOMAC.

Table 6
Comparison of FOMAC with other adsorbents for Pb(II) removal.

Adsorbent material	Adsorption capacity (mg/g)	References
Sugarcane bagasse	0.094	[66]
Brewed tea waste	1.197	[67]
Activated carbon	6.27	[68]
Hydrophilic carbonaceous nanoparticles (SHNPs)	8.87	[69]
Waste rubber tires	9.6805	[70]
Food-grade κ-carrageenan beads	5.48	[71]
Hydrochar pinewood sawdust	2.20	[72]
Agave bagasse	10.9	[73]
sludge-based biochar	7.56	[74]
Fe_3O_4/MgO/AC (FOMAC)	11.121	This study

Table 7
Comparison of FOMAC with other adsorbents for Cd(II) removal.

Adsorbent material	Adsorption capacity (mg/g)	References
Sugarcane bagasse	0.11	[66]
Brewed tea waste	2.468	[67]
Hyewdrophilic carbonaceous nanoparticles (SHNPs)	0.54	[69]
Chitosan and coffee powder	0.9970	[74]
Granular sludge-clay	1.53	[75]
Polyamide	1.70 ± 0.04	[76]
Polyvinyl chloride	1.04 ± 0.03	[76]
Polystyrene	0.76 ± 0.02	[76]
Acrylonitrile butadiene styrene	0.25 ± 0.01	[76]
Fe_3O_4/MgO/AC (FOMAC)	3.053	This study

4. Conclusions

FOMAC was successfully synthesized from natural iron sand and coconut shell with unique characteristics in the form of an inverse cubic spinel structure for Fe_3O_4 and a face-centered cubic structure for MgO with crystallite sizes of 12.85 nm and 36.06 nm, respectively. Furthermore, FOMAC has spherical and chunk morphology at the nanoscale. The formation of FOMAC was also indicated by the emergence of functional groups of Fe–O, Mg–O, and C=C, suggesting effective interactions among the constituent materials. FOMAC also has a high specific surface area of 30.6802 m^2/g and superparamagnetic behavior with a saturation magnetization of 10.006 emu/g, which facilitates separation after adsorption. Interestingly, FOMAC demonstrated bifunctional performance in environmental remediation with strong antibacterial activity, forming inhibition zones of 12.49 mm against *E. coli* and 14.10 mm against *S. aureus*, as well as outstanding heavy metal removal capabilities of 63.40% for Pb(II) and 98.83% for Cd(II). Thus, the final findings suggest that FOMAC can play a dual role as an adsorbent for heavy metals Pb(II) and Cd(II) and as an antibacterial agent in aquatic systems, making water more suitable for humans and other living things.

CRediT authorship contribution statement

Taufiq Ahmad: Writing – review & editing, Supervision, Project administration, Funding acquisition, Conceptualization. **Fen Yap Wing:** Writing – review & editing, Methodology, Data curation. **Amrillah Tahta:** Writing – review & editing, Visualization, Methodology. **Hidayat Nurul:** Validation, Methodology, Formal analysis. **Zhafirah Aura Gitta:** Resources, Methodology, Investigation. **Rokhimah Alfi Qoidatu:** Resources, Methodology, Investigation. **Rahmawati Febriana:** Visualization, Methodology, Investigation. **Setiana Mina Devika:** Writing – original draft, Investigation, Data curation. **Zainullah Muhammad:** Writing – original draft, Visualization, Resources, Investigation.

Declaration of Competing Interest

The authors declare no competing financial or personal interests that could influence this work.

Acknowledgements

This work was supported by Kemdiktisaintek Republik Indonesia and Universitas Negeri Malang for AT.

References

[1] R. Kaveh, M. Bagherzadeh, Simultaneous Removal of Mercury Ions and Cationic and Anionic Dyes from Aqueous Solution using Epichlorohydrin Cross-Linked Chitosan@Magnetic (Fe_3O_4)/Activated Carbon Nanocomposite as an Adsorbent, Diam. Relat. Mater. 124 (Apr. 2022) 108923, https://doi.org/10.1016/j.diamond.2022.108923.
[2] K. Raj, A.P. Das, Lead Pollution: Impact on Environment and Human Health and Approach for a Sustainable Solution, Environ. Chem. Ecotoxicol. 5 (2023) 79–85, https://doi.org/10.1016/j.enceco.2023.02.001.
[3] D. Puthran, D. Patil, Usage of Heavy Metal-Free Compounds in Surface Coatings, J. Coat. Technol. Res 20 (1) (Jan. 2023) 87–112, https://doi.org/10.1007/s11998-022-00648-4.
[4] Y. Zhang, B. Wang, Q. Cheng, X. Li, Z. Li, Removal of Toxic Heavy Metal Ions (Pb, Cr, Cu, Ni, Zn, Co, Hg, and Cd) from Waste Batteries or Lithium Cells Using Nanosized Metal Oxides: A Review, J. Nanosci. Nanotechnol. 20 (12) (Dec. 2020) 7231–7254, https://doi.org/10.1166/jnn.2020.18748.
[5] N.P. Castro González, F. Calderón Sánchez, G.J. Pérez Marroquín, Spatial Analysis of Heavy Metals in Agricultural Soils of the Atoyaczahuapan Sub-Basin and Risks to Public Health, Agric. Soc. Y. Desarro. 21 (1) (Dec. 2023), https://doi.org/10.22231/asyd.v21i1.1593.
[6] T. Liu, et al., Adsorption of Cadmium and Lead from Aqueous Solution using Modified Biochar: A Review, J. Environ. Chem. Eng. 10 (1) (Feb. 2022) 106502, https://doi.org/10.1016/j.jece.2021.106502.
[7] M. Vesali-Naseh, M.R. Vesali Naseh, P. Ameri, Adsorption of Pb(II) Ions from Aqueous Solutions using Carbon Nanotubes: A Systematic Review, J. Clean. Prod. 291 (Apr. 2021) 125917, https://doi.org/10.1016/j.jclepro.2021.125917.
[8] World Health Organzation (WHO), "Almost 1 Million People Die Every Year Due to Lead Poisoning, with More Children Suffering Long-Term Health Effects," World

Health Organization (WHO). Accessed: Dec. 02, 2024. [Online]. Available: ⟨https://www.who.int/news/item/23-10-2022-almost-1-million-people-die-every-year-due-to-lead-poisoning–with-more-children-suffering-long-term-health-effects#:~:text=Each%20year%2C%20an%20estimated%201,toxicity%20to%20the%20reproductive%20organs⟩.

[9] A.E. Charkiewicz, W.J. Omeljaniuk, K. Nowak, M. Garley, and J. Nikliński, "Cadmium Toxicity and Health Effects—A Brief Summary," Sep. 01, 2023, *Multidisciplinary Digital Publishing Institute (MDPI)*. doi: 10.3390/molecules28186620.

[10] K. Ahmad, et al., Lead in Drinking Water: Adsorption Method and Role of Zeolitic Imidazolate Frameworks for its Remediation: A Review, J. Clean. Prod. 368 (Sep. 2022) 133010, https://doi.org/10.1016/j.jclepro.2022.133010.

[11] B. Tessema, G. Gonfa, S. Mekuria Hailegiorgis, M. Tesfaye Gari, Synthesis and Characterization of Modified Silica Gel Supported Silver Nanoparticles using Batch Studies for Disinfection of *Escherichia coli* and *Staphylococcus aureus* for Drinking Water, J. Mater. Process Technol. 1 (2) (Dec. 2024) 64–78, https://doi.org/10.69660/jmpt.v1i2.86.

[12] M. Yadav, G. Singh, R.N. Jadeja, Physical and Chemical Methods for Heavy Metal Removal, Pollutants and Water Management, Wiley, 2021, pp. 377–397, https://doi.org/10.1002/9781119693635.ch15.

[13] R. Shrestha, et al., Technological Trends in Heavy Metals Removal from Industrial Wastewater: A Review, J. Environ. Chem. Eng. 9 (4) (2021) 105668–105686, https://doi.org/10.1016/j.jece.2021.105688.

[14] M. Cai, Y. Liu, K. Dong, X. Chen, S. Li, Floatable S-Scheme Bi_2WO_6/C_3N_4/Carbon Fiber Cloth Composite Photocatalyst for Efficient Water Decontamination, Chin. J. Catal. 52 (Sep. 2023) 239–251, https://doi.org/10.1016/S1872-2067(23)64496-1.

[15] S. Li, C. Wang, K. Dong, P. Zhang, X. Chen, X. Li, MIL-101(Fe)/BiOBr S-Scheme Photocatalyst for Promoting Photocatalytic Abatement of Cr(VI) and Enrofloxacin Antibiotic: Performance and Mechanism, Chin. J. Catal. 51 (Aug. 2023) 101–112, https://doi.org/10.1016/S1872-2067(23)64479-1.

[16] R. Shrestha, et al., Technological Trends in Heavy Metals Removal from Industrial Wastewater: A review, J. Environ. Chem. Eng. 9 (4) (Aug. 2021) 105688, https://doi.org/10.1016/j.jece.2021.105688.

[17] S. Li, M. Cai, Y. Liu, C. Wang, R. Yan, X. Chen, Constructing $Cd_{0.5}Zn_{0.5}S/Bi_2WO_6$ S-Scheme Heterojunction for Boosted Photocatalytic Antibiotic Oxidation and Cr(VI) Reduction, Adv. Powder Mater. 2 (1) (Jan. 2023) 100073, https://doi.org/10.1016/j.apmate.2022.100073.

[18] Z.-Y. He, H. Liu, Inactivation Mechanisms of Intracellular Coliphages in host Bacteria by Chemical Disinfection with Ozone, Chlorine Oxide, Chlorine and Chloramine, Water Res 287 (Dec. 2025) 124404, https://doi.org/10.1016/j.watres.2025.124404.

[19] M. Namvar-Mahboub, E. Khodeir, M. Bahadori, S.M. Mahdizadeh, Preparation of magnetic MgO/Fe_3O_4 via the green method for competitive removal of Pb and Cd from aqueous solution, Colloids Surf. A Physicochem Eng. Asp. 589 (Feb. 2020) 124419, https://doi.org/10.1016/j.colsurfa.2020.124419.

[20] R. Alrowais, M.M. Abdel daiem, B.M. Nasef, N. Said, Activated Carbon Fabricated from Biomass for Adsorption/Bio-Adsorption of 2,4-D and MCPA: Kinetics, Isotherms, and Artificial Neural Network Modeling, Sustainability 16 (1) (Dec. 2023) 299, https://doi.org/10.3390/su16010299.

[21] R. Haider, et al., Sustainable Activated Carbon Derived from Coconut Shell and Betel Nuts for Energy Storage and Environmental Remediation, Diam. Relat. Mater. 154 (Apr. 2025) 112243, https://doi.org/10.1016/j.diamond.2025.112243.

[22] X. Rong, et al., Performance Optimization and Kinetic Analysis of HNO_3 Coupled with Microwave Rapidly Modified Coconut Shell Activated Carbon for VOCs Adsorption, Front Energy Res 10 (Jan. 2023), https://doi.org/10.3389/fenrg.2022.1047254.

[23] O.E.D. Artika, R. Yulistiani, Minimum Inhibitory Concentration of Chitosan and Coconut Shell Liquid Smoke Against *Staphylococcus aureus* and *Escherichia coli*, AJARCDE (Asian Journal Applied Research Community Development Empowerment 9 (3) (Nov. 2025) 182–187, https://doi.org/10.29165/ajarcde.v9i3.811.

[24] X. Ma, et al., MOFs Meet Wood: Reusable Magnetic Hydrophilic Composites Toward Efficient Water Treatment with Super-High Dye Adsorption Capacity at High Dye Concentration, Chem. Eng. J. 446 (Oct. 2022) 136851, https://doi.org/10.1016/j.cej.2022.136851.

[25] A.N. Syahida, et al., Diffraction and Magnetization Properties of Fe_3O_4 Nanoparticle from Natural Iron Sand in Various Stirring Rate for Potential Biomedical Applications, Rasayan J. Chem. 15 (01) (2022) 316–325, https://doi.org/10.31788/RJC.2022.1516615.

[26] S.R. Metta, U.K. Sahu, Removal of Cr(VI) from Aqueous Solution Using Magnetic Activated Carbon Prepared from Waste Shell of Marigold Flower Straw: Kinetics, Isotherm and Mechanism Studies, AUIQ Complement. Biol. Syst. 2 (1) (Mar. 2025) 77–89, https://doi.org/10.70176/3007-973X.1025.

[27] A. Wahfiudin, et al., Parameters Adjustments for Facile Synthesis of High Magnetization Iron Oxide Nanoparticles from Natural Sand, NanoStruct. & NanoObjects 37 (Feb. 2024) 101114, https://doi.org/10.1016/j.nanoso.2024.101114.

[28] M. Shahrashoub, S. Bakhtiari, The Efficiency of Activated Carbon/Magnetite Nanoparticles Composites in Copper Removal: Industrial Waste Recovery, Green Synthesis, Characterization, and Adsorption-Desorption Studies, Microporous Mesoporous Mater. 311 (Feb. 2021) 110692, https://doi.org/10.1016/j.micromeso.2020.110692.

[29] M. Rukhsar, Z. Ahmad, A. Rauf, H. Zeb, M. Ur-Rehman, H.A. Hemeg, An Overview of Iron Oxide (Fe_3O_4) Nanoparticles: From Synthetic Strategies, Characterization to Antibacterial and Anticancer Applications, Cryst. (Basel) 12 (12) (Dec. 2022) 1809, https://doi.org/10.3390/cryst12121809.

[30] M. Ramadhan, F. Fahmiati, A. Alrum, M.L.O.M. Zuhdi, Free Solvent Isolation of Fe3O4 from Magnetic Material Iron Sand Utilizing High-Energy Ball Milling as Adsorben Remazol Turquoise Blue G-133 and Remazol Red RB-133, Acta Chim. Asian 6 (1) (2023) 269–278.

[31] Q. Gao, Y. Shen, X. Jiang, H. Zheng, F. Shen, C. Liu, Effect of MgO on Oxidation Process of Fe_3O_4 in Pellets, J. Iron Steel Res. Int. 23 (10) (Oct. 2016) 1007–1011, https://doi.org/10.1016/S1006-706X(16)30151-0.

[32] Y. Wang, J. Zhang, L. Niu, Z. Liu, H. Jiang, Inhibition Mechanism of MgO Addition on High-Temperature Oxidation of Magnetite: Density Functional Theory and Ab Initio Molecular Dynamics Methods Joint Research and Experimental Verification, Steel Res Int 94 (8) (Aug. 2023), https://doi.org/10.1002/srin.202200887.

[33] D.-M. Radulescu, et al., Green-Synthesized MgO Nanoparticles: Structural Insights and Antimicrobial Applications, Int J. Mol. Sci. 26 (18) (Sep. 2025) 9021, https://doi.org/10.3390/ijms26189021.

[34] Z. Feng, N. Chen, T. Liu, C. Feng, $KHCO_3$ Activated Biochar Supporting MgO for Pb (II) and Cd(II) Adsorption from Water: Experimental Study and DFT Calculation Analysis, J. Hazard Mater. 426 (Mar. 2022) 128059, https://doi.org/10.1016/j.jhazmat.2021.128059.

[35] A. Al-Sharabi, K.S.S. Sada'a, A. AL-Osta, R. Abd-Shukor, Structure, Optical Properties, and Antimicrobial Activities of $MgO–Bi_{2-x}Cr_xO_3$ nanocomposites prepared via solvent-deficient method, Sci. Rep. 12 (1) (Jun. 2022) 10647, https://doi.org/10.1038/s41598-022-14811-9.

[36] M. Hanif, et al., A Wide Bandgap $Ag/MgO@Fe_3O_4$Nanocomposite as Magnetic Sorbent for Cd(II) in Water Samples, Curr. Anal. Chem. 16 (3) (May 2020) 332–340, https://doi.org/10.2174/1573411015666191205102628.

[37] H. Esmaeili, S.M. Mousavi, S.A. Hashemi, W.-H. Chiang, S. Ahmadpour Abnavi, Activated $Carbon@MgO@Fe_3O_4$ as an Efficient Adsorbent for As(III) Removal, Carbon Lett. 31 (5) (Oct. 2021) 851–862, https://doi.org/10.1007/s42823-020-00186-2.

[38] K.K. Zadeh, D. Jafari, Activated Carbon/Alginate/Fe_3O_4 Magnetic Nanocomposite as a Superior Functional Material for Removal of Lead from Aqueous Media, Biomass.. Convers. Biorefin 14 (16) (Aug. 2024) 19025–19043, https://doi.org/10.1007/s13399-023-04040-z.

[39] G. Aydin, E.B. Zorlu, Characterisation and Antibacterial Properties of Novel Biodegradable Films Based on Alginate and Roselle (*Hibiscus sabdariffa* L.) Extract, Waste Biomass.. Valoriz. 13 (6) (Jun. 2022) 2991–3002, https://doi.org/10.1007/s12649-022-01710-3.

[40] M.H. Fekri, S.I. Mohamareh, M. Hosseini, M.R. Mehr, Green Synthesis of Activated carbon/Fe_3O_4 Nanocomposite from Flaxseed and its Application as Adsorbent and Antibacterial Agent, Chem. Pap. 76 (11) (Nov. 2022) 6767–6782, https://doi.org/10.1007/s11696-022-02278-x.

[41] L.B. Anigol, V.P. Sajjan, P.M. Gurubasavaraj, Evaluation of Antioxidant and Antibacterial Property of Microwave Assisted Green Synthesis of Fe_3O_4-MgO Nanocomposites, Indian J. Sci. Technol. 16 (24) (Jun. 2023) 1777–1786, https://doi.org/10.17485/IJST/v16i24.629.

[42] A. Taufiq, et al., Synthesis of Fe_3O_4/Ag Nanohybrid Ferrofluids and Their Applications as Antimicrobial and Antifibrotic Agents, J. Heliyon 6 (12) (2020) 05813, https://doi.org/10.1016/j.heliyon.2020.e05813.

[43] B.R. Mphuthi, P.M. Thabede, J.S. Modise, T. Xaba, N.D. Shooto, Adsorption of Cadmium and Methylene Blue Using Highly Porous Carbon from Hemp Seeds, Appl. Sci. 13 (17) (Aug. 2023) 9659, https://doi.org/10.3390/app13179659.

[44] M.R. Bindhu, M. Umadevi, M. Kavin Micheal, M.V. Arasu, N. Abdullah Al-Dhabi, Structural, Morphological and Optical Properties of MgO Nanoparticles for Antibacterial Applications, Mater. Lett. 166 (Mar. 2016) 19–22, https://doi.org/10.1016/j.matlet.2015.12.020.

[45] P. Hu, et al., High Saturation Magnetization Fe_3O_4 Nanoparticles Prepared by One-Step Reduction Method in Autoclave, J. Alloy. Compd. 728 (Dec. 2017) 88–92, https://doi.org/10.1016/j.jallcom.2017.08.290.

[46] X.-L. Cheng, J.-S. Jiang, D.-M. Jiang, Z.-J. Zhao, Synthesis of Rhombic Dodecahedral Fe_3O_4 Nanocrystals with Exposed High-Energy {110} Facets and Their Peroxidase-like Activity and Lithium Storage Properties, J. Phys. Chem. C. 118 (24) (Jun. 2014) 12588–12598, https://doi.org/10.1021/jp412661e.

[47] A. N, B. C. Ang, A. M.A, C.W. Bong, Influence of Precursor Concentration and Temperature on the Formation of Nanosilver in Chemical Reduction Method, Sains Malays. 47 (1) (Jan. 2018) 157–168, https://doi.org/10.17576/jsm-2018-4701-19.

[48] V. Priyan V, N. Kumar, S. Narayanasamy, Toxicological Assessment and Adsorptive Removal of Lead (Pb) and Congo Red (CR) from Water by Synthesized Iron Oxide/Activated Carbon (Fe_3O_4/AC) Nanocomposite, Chemosphere 294 (May 2022) 133758, https://doi.org/10.1016/j.chemosphere.2022.133758.

[49] E. Asuquo, A. Martin, P. Nzerem, F. Siperstein, X. Fan, Adsorption of Cd(II) and Pb (II) Ions from Aqueous Solutions using Mesoporous Activated Carbon Adsorbent: Equilibrium, Kinetics and Characterisation Studies, J. Environ. Chem. Eng. 5 (1) (2017) 679–698, https://doi.org/10.1016/j.jece.2016.12.043.

[50] K. Duraisamy, et al., Single domain soft ferromagnetic ferrofluid suitable for intratumoural magnetic hyperthermia, no. August 2023, Colloids Surf. A Physicochem Eng. Asp. 684 (2024) 133049, https://doi.org/10.1016/j.colsurfa.2023.133049.

[51] N.G. Mele, A.M. Güerci, G.A. Pasquevich, Cytotoxicity and genotoxicity of citric acid coated magnetite/maghemite nanoparticles in human lung cancer cells, J. Magn. Magn. Mater. 592 (no. January, 2024), https://doi.org/10.1016/j.jmmm.2024.171784.

[52] M.A.S. Amulya, H.P. Nagaswarupa, M.R.A. Kumar, C.R. Ravikumar, K.B. Kusuma, S.C. Prashantha, Evaluation of bifunctional applications of $CuFe_2O_4$ nanoparticles synthesized by a sonochemical method, no. February 2020, J. Phys. Chem. Solids 148 (2021) 109756, https://doi.org/10.1016/j.jpcs.2020.109756.

[53] N. Masunga, B.B. Mamba, Y.W. Getahun, A.A. El-Gendy, K.K. Kefeni, Synthesis of single-phase superparamagnetic copper ferrite nanoparticles using an optimized coprecipitation method (no. January), Materials Science Engineering B 272 (2021) 115368, https://doi.org/10.1016/j.mseb.2021.115368.
[54] S.A. Aldahash, P. Higgins, S. Siddiqui, M.K. Uddin, Fabrication of Polyamide-12/Cement Nanocomposite and its Testing for Different Dyes Removal from Aqueous Solution: Characterization, Adsorption, and Regeneration Studies, Sci. Rep. 12 (1) (Jul. 2022) 13144, https://doi.org/10.1038/s41598-022-16977-8.
[55] L. Hakim, E. Sedyadi, Synthesis and Characterization of Fe_3O_4 Composites Embeded on Coconut Shell Activated Carbon, JKPK (J. Kim. Dan. Pendidik. Kim.) 5 (3) (Dec. 2020) 245, https://doi.org/10.20961/jkpk.v5i3.46543.
[56] M. Negi, V. Thankachan, A. Rajeev, M. Vairamuthu, S. Arundhathi, P.V. Nidheesh, Clean and Green Bamboo Magic: Recent Advances in Heavy Metal Removal from Water by Bamboo Adsorbents, Water (Basel) 17 (3) (Feb. 2025) 454, https://doi.org/10.3390/w17030454.
[57] Y. Yang, et al., Construction of $CoFe_2O_4/Fe_2O_3$ S-Type Heterojunctions on Biochar for Activating Peroxymonosulfate Towards Simultaneous Removal of TC and Cr (VI), Sep Purif. Technol. 354 (Feb. 2025) 129157, https://doi.org/10.1016/j.seppur.2024.129157.
[58] CLSI, "Performance Standards for Antimicrobial Susceptibility Testing. Edisi ke-30," CLSI. Accessed: Aug. 08, 2024. [Online]. Available: 〈https://clsi.org/media/3481/m100ed30_sample.pdf〉.
[59] F. Gao, T. Shao, Y. Yu, Y. Xiong, L. Yang, Surface-Bound Reactive Oxygen Species Generating Nanozymes for Selective Antibacterial Action, Nat. Commun. 12 (1) (Feb. 2021) 745, https://doi.org/10.1038/s41467-021-20965-3.
[60] W. Huang, et al., Effect Analysis of Pore Wall Thickness, Pore Size, and Functional Group of Activated Carbon on Adsorption Behavior Based on Molecular Simulation, Environ. Sci. Pollut. Res. 28 (42) (Nov. 2021) 59908–59924, https://doi.org/10.1007/s11356-021-14355-x.
[61] M. Du, et al., Insight into the Synthesis and Adsorption Mechanism of Adsorbents for Efficient Phosphate Removal: Exploration from Synthesis to Modification, Chem. Eng. J. 442 (Aug. 2022) 136147, https://doi.org/10.1016/j.cej.2022.136147.
[62] C.E.R. Barquilha, M.C.B. Braga, Adsorption of Organic and Inorganic Pollutants Onto Biochars: Challenges, Operating Conditions, and Mechanisms, Bioresour. Technol. Rep. 15 (Sep. 2021) 100728, https://doi.org/10.1016/j.biteb.2021.100728.
[63] V. Bernal, A. Erto, L. Giraldo, J. Moreno-Piraján, Effect of Solution pH on the Adsorption of Paracetamol on Chemically Modified Activated Carbons, Molecules 22 (7) (Jun. 2017) 1032, https://doi.org/10.3390/molecules22071032.
[64] S. Rajendran, et al., A Critical and Recent Developments on Adsorption Technique for Removal of Heavy Metals from Wastewater-A Review, Chemosphere 303 (Sep. 2022) 135146, https://doi.org/10.1016/j.chemosphere.2022.135146.
[65] T.P. Fato, D.-W. Li, L.-J. Zhao, K. Qiu, Y.-T. Long, Simultaneous Removal of Multiple Heavy Metal Ions from River Water Using Ultrafine Mesoporous Magnetite Nanoparticles, ACS Omega 4 (4) (Apr. 2019) 7543–7549, https://doi.org/10.1021/acsomega.9b00731.
[66] L.M. Vera, D. Bermejo, M.F. Uguña, N. Garcia, M. Flores, E. González, Fixed Bed Column Modeling of Lead(II) and Cadmium(II) Ions Biosorption on Sugarcane Bagasse, Environ. Eng. Res. 24 (1) (May 2018) 31–37, https://doi.org/10.4491/eer.2018.042.
[67] H. Çelebi, G. Gök, O. Gök, Adsorption Capability of Brewed Tea Waste in Waters Containing Toxic Lead(II), Cadmium (II), Nickel (II), and Zinc(II) Heavy Metal Ions, Sci. Rep. 10 (1) (Oct. 2020) 17570, https://doi.org/10.1038/s41598-020-74553-4.
[68] M.D. Yahya, K.S. Obayomi, M.B. Abdulkadir, Y.A. Iyaka, A.G. Olugbenga, Characterization of Cobalt Ferrite-Supported Activated Carbon for Removal of Chromium and Lead Ions from Tannery Wastewater via Adsorption Equilibrium, Water Sci. Eng. 13 (3) (Sep. 2020) 202–213, https://doi.org/10.1016/j.wse.2020.09.007.
[69] F. Di Natale, V. Gargiulo, M. Alfè, Adsorption of Heavy Metals on Silica-Supported Hydrophilic Carbonaceous Nanoparticles (SHNPs), J. Hazard Mater. 393 (Jul. 2020) 122374, https://doi.org/10.1016/j.jhazmat.2020.122374.
[70] F. Cherono, N. Mburu, B. Kakoi, Adsorption of Lead, Copper and Zinc in a Multi-Metal Aqueous Solution by Waste Rubber Tires for the Design of Single Batch Adsorber, Heliyon 7 (11) (Nov. 2021) e08254, https://doi.org/10.1016/j.heliyon.2021.e08254.
[71] F.P. Hilmawan, K.R. Amalia, M. Iqbal, S. Chairurrizky, U. Triadhi, Kinetic Study of Pb(II) Adsorption on Food-grade κ-Carrageenan Beads, J. Serambi Eng. 9 (3) (2024) 10193–10200.
[72] Y. Xia, et al., Enhanced Adsorption of Pb(II) onto Modified Hydrochar: Modeling and Mechanism Analysis, Bioresour. Technol. 288 (Sep. 2019) 121593, https://doi.org/10.1016/j.biortech.2019.121593.
[73] D. Cholico-González, N. Ortiz Lara, A.M. Fernández Macedo, J. Chavez Salas, Adsorption Behavior of Pb(II), Cd(II), and Zn(II) onto Agave Bagasse, Characterization, and Mechanism, ACS Omega 5 (7) (Feb. 2020) 3302–3314, https://doi.org/10.1021/acsomega.9b03385.
[74] J. Zhang, et al., Effect of Deashing on Activation Process and Lead Adsorption Capacities of Sludge-Based Biochar, Sci. Total Environ. 716 (May 2020) 137016, https://doi.org/10.1016/j.scitotenv.2020.137016.
[75] X. Du, S. Cui, X. Fang, Q. Wang, G. Liu, Adsorption of Cd(II), Cu(II), and Zn(II) by Granules Prepared using Sludge from a Drinking Water Purification Plant, J. Environ. Chem. Eng. 8 (6) (Dec. 2020) 104530, https://doi.org/10.1016/j.jece.2020.104530.
[76] Y. Zhou, Y. Yang, G. Liu, G. He, W. Liu, Adsorption Mechanism of Cadmium on Microplastics and their Desorption Behavior in Sediment and Gut Environments: The Roles of water pH, Lead Ions, Natural Organic Matter and Phenanthrene, Water Res 184 (Oct. 2020) 116209, https://doi.org/10.1016/j.watres.2020.116209.